Measurement of methane, nitrous oxide and ammonia in atmosphere with a compact quartz-enhanced photoacoustic sensor

Measurement of methane, nitrous oxide and ammonia in atmosphere with a compact quartz-enhanced photoacoustic sensor

Giansergio Menduni[a], Andrea Zifarelli[a], Elena Kniazeva[a], Stefano Dello Russo[b], Pietro Patimisco[a] Angelo Sampaolo[a], Marilena Giglio[a], Fabrizio Manassero[c], Elio Dinuccio[d], Giorgio Provolo[e], Vincenzo Spagnolo[a]

[a] PolySense Lab - Dipartimento Interateneo di Fisica, Politecnico and University of Bari, Via Amendola 173, Bari, Italy;
[b] Italian Space Agency (ASI), Centro di geodesia Spaziale "Giuseppe Colombo", Matera, Italy;
[c] ETG Risorse e Tecnologie Srl, Via Padre Carpignano 23, Montiglio Monferrato, Asti, Italy;
[d] Department of Agriculture, Forest and Food Science - Div. Agro-Forestry and Environmental Engineering - University of Turin, Largo Paolo Braccini 2, Grugliasco 10095 (TO), Italy;

[e] Department of Agricultural and Environmental Sciences, Production, Landscape, Agroenergy, University of Milan, Via Celoria 2, Milano 20133, Italy.

ABSTRACT

We report on a compact and portable 19-inches 6U-rack sensor for simultaneous detection of methane, nitrous oxide, and ammonia in atmosphere. The sensor embeds two detection modules based on quartz-enhanced photoacoustic spectroscopy, each one equipped with a quantum cascade laser as light source and a spectrophone exploiting custom-made quartz tuning fork. Dedicated electronic boards were designed to control the laser sources, stabilize the gas flow and perform data analysis, with a computer interface for an easy end-user operation. The sensor was calibrated in laboratory environment with certified concentrations. At 0.1 s signal integration time, detection limits of 28.0 ppb, 8.6 ppb and 5.8 ppb were obtained for CH_4, N_2O and NH_3 respectively. Since these detection limits were well below the natural abundance of the three analytes in atmosphere, the sensor was employed to monitor CH_4, N_2O and NH_3 concentrations in laboratory air.

Keywords: quartz-enhanced photoacoustic spectroscopy, trace gas sensing, methane, nitrous oxide, ammonia, multi-gas detection.

1. INTRODUCTION

With an increasing human population, and the consequent need for more food production, a major challenge for agriculture is the decrease in the environmental footprint. Indeed, agriculture strongly contributes to global environmental change, mainly through emissions of greenhouse gases (GHG). The GHGs danger is measured by their global warming potential (GWP) that quantifies the heat trapping potential of each GHG relative to that of carbon dioxide. Methane (CH_4) and nitrous oxide (N_2O) are the most important non-CO_2 GHGs emitted and are characterized by GWPs 25 and 265 times higher than CO_2, respectively [1, 2]. Both pollutants predominantly come from enteric fermentation produced in the natural part of digestive systems of ruminants, anaerobic decomposition of organic matter in paddy fields emitted by rice cultivation, application and storage of manure and burning of biomass vegetation and crop residues [3, 4]. Furthermore, the use of animal manure and nitrogen fertilizers in grain crops production increase the emission of ammonia (NH_3), contributing to the formation of fine particulate matter, which is considered a major public health concern [5]. Gaseous ammonia has a relatively short lifetime in the atmosphere ranging from a few hours to a few days [6] and is deposited quite close to its source [7]. Typical levels of ammonia can range from concentrations lower than part-per-billion (ppb), up to several part-per-million (ppm) near animal waste lagoons and animal stalls [8]. Accordingly, the detection of traces of ammonia in the atmosphere is of interest from both an environmental and a physical point of view.

With the aim to better understand the global warming and the impact on the environment, highly precise and sensitive gas sensors are necessary to determine the source and concentration levels of CH_4, N_2O and NH_3. To fulfil the above requirements, optical techniques based on tunable diode laser absorption spectroscopy are the most appropriate methods [9]. Highly performant mid-infrared absorption spectrometers for high precision measurements uses quantum cascade lasers (QCLs) as light source to target absorption lines of fundamental bands, with optical powers of several tens of milliwatt. The compactness and the robustness that confer the possibility of a sensor to be employed for in-field operation are determined by the employed gas cell and the capability to preserve over long times the optical alignment between the laser beam and the gas cell. The two types of gas cell that guarantee high stability are the multipass cell and the photoacoustic cell. Multipass cells trap laser beam into multiple reflections between two large diameter focusing mirrors. Optical pathlengths as high as 50 m can be reached with gas cell lengths of few tens of centimeters [10]. Many robust portable sensors employing multipass cells and expensive fast infrared detectors were demonstrated and developed over the last years [11, 12]. By squeezing the cell, the effective pathlength is reduced, making impossible to realize efficient multipass cells with physical size of less than 10 cm. Photoacoustic cells are acoustic resonators that amplify the weak sound waves generated by photoacoustic effect occurring within an absorbing gas. The optical alignment is easy, and a microphone is placed at the antinode point of the amplified acoustic pattern within the cell [13]. For Helmholtz acoustic resonators, a normal acoustic mode of few kHz imposes sizes of 10-20 cm for the gas cell. Moreover, the use of microphone requires a rigid acoustic isolation for the external ambient noise. Starting from 2002, an alternative to traditional microphones is represented by quartz tuning forks (QTF) which operate as sharply resonant acoustic transducers [14, 15]. This variant of the photoacoustic spectroscopy is named as Quartz-Enhanced Photoacoustic Spectroscopy (QEPAS). The QTF is placed within the gas cell, and it is coupled with a pair of millimeter-size resonator tubes acting as organ pipes. As a result, the gas cell only serves to separate the sample to be analyzed from the external ambient, allowing volumes of few cubic centimeters [16], thus removing restrictions imposed on the gas cell size by the acoustic resonance conditions [17, 18].. The laser beam passes through the resonator tubes, between the prongs of the QTF, and is modulated at the QTF resonance frequency or at one of its subharmonics. Due to photoacoustic effect, the sound wave generated between the prongs of the QTF puts them into vibration: the prongs' mechanical deflection is converted into an electrical signal thanks to the piezoelectricity of the quartz [19]. Thus, QEPAS can face up to requirements to perform reliable measurements of different gases through a modular assembly of centimeter-sizes multiple detection modules into one portable system.

Here we report on the realization of a compact sensing system composed of two QEPAS sensor-heads (SH). Each sensor-head contains the laser source and a spectrophone composed by a quartz tuning fork resonant at 12.4 kHz and a pair of acoustic resonator tubes. One sensor-head targets two adjacent but not superimposed spectral lines of CH_4 and N_2O centered at 1275.04 cm^{-1} and 1275.49 cm^{-1} respectively, while the other one aims at a NH_3 absorption line falling at 1103.44 cm^{-1}. The two sensor-heads were embedded into a compact system equipped with control boards to simultaneously drive both laser sources, as well as to retrieve and analyze the spectrophone signals. It also allows to set the gas pressure and measure its flow.

2. QUARTZ-ENHANCED PHOTOACOUSTIC SENSOR BOX

The sensor is composed of two sensor-heads with the respective gas lines connected in series, all embedded in a box, as schematically depicted in Fig. 1a. A picture of the final 19-inches 6U-rack sensor system which includes two chemical sensors to measure also CO_2 and H_2O concentrations, is also shown in Fig. 1b.

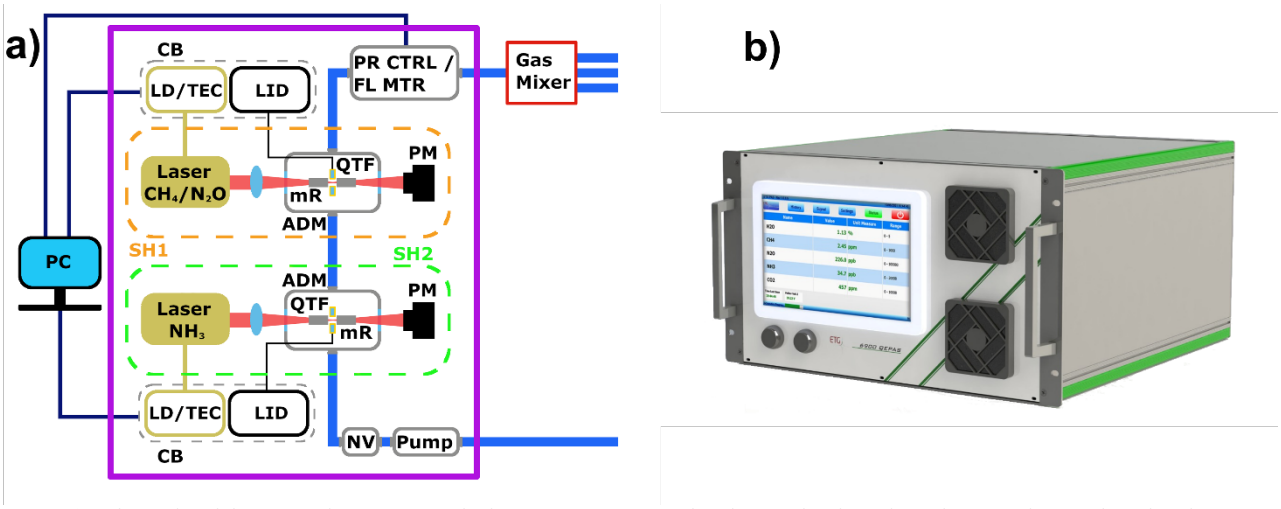

Fig. 1. a) Schematic of the sensor box composed of two QEPAS sensor heads, one for detection of CH_4 and N_2O, the other for NH_3 detection, connected in series in the same gas line. b) Picture of the realized 19-inches 6U-rack sensor. Size: 35cmx55cmx44cm, weight 14 kg. PC – Personal Computer; QTF – Quartz Tuning Fork; mR – Resonator tubes; ADM – Acoustic Detection Module; PM – Power Meter; SH1 – Sensor Head 1; SH2 – Sensor Head 2; CB – Control Board; LD – Laser Driver; TEC – Thermoelectric Cooler; LID – Lock-In Detection; PR CTRL/FL MTR – Pressure controller/ Flow Meter; NV – Needle Valve.

The optical components of a QEPAS sensor are placed inside the SH, improving the robustness to misalignment, and reducing its overall dimensions. Each SH is composed of a quantum cascade laser (QCL), a ZnSe lens with a focal length of 40 mm, an acoustic detection module (ADM) and an optical power meter (THORLABS PM100USB) for alignment purposes. The ADM consists of a spectrophone enclosed in a compact vacuum-tight gas cell equipped with two windows and inlet/outlet gas connectors. The spectrophone is composed of a T-shaped QTF acoustically coupled with a pair of resonator tubes having a length of 12.4 mm and an inner diameter of 1.59 mm. This configuration has proven to provide the highest signal to noise ratio enhancement with respect to the bare QTF [20, 21]. For each SH, the collimated laser beam is focused into the ADM, passing through the resonator tubes and between the QTF prongs. When the laser wavelength is modulated and tuned to an absorption feature, the photoacoustic effect occurs, and a standing wave vibrational pattern is created within the spectrophone. SH1 mounts a QCL (Thorlabs QD7840HHLH-A) which targets two adjacent absorption features of CH_4, centered at 1275.04 cm^{-1} and 1275.39 cm^{-1} with their respective linestrengths of $3.73 \cdot 10^{-20}$ cm/molecule and $2.48 \cdot 10^{-20}$ cm/molecule, and an absorption feature of N_2O, centered at 1275.49 cm^{-1} with a linestrength of $1.42 \cdot 10^{-19}$ cm/molecule [22].

In SH2, the laser source is a QCL (Thorlabs QD9062HHLH-C), capable to target the absorption line of NH_3 at 1103.44 cm^{-1}, having a linestrength of $1.51 \cdot 10^{-19}$ cm/molecule [22]. The QCLs injection currents and temperatures were controlled by the Merstetter Engineering LTC-1141 control boards (CB). For SH1, the QCL temperature was fixed at 20 °C to target the 1275.04 cm^{-1} CH_4 line at an injected current of 319 mA with an optical power of 74 mW, and the N_2O line at 340 mA with an optical power of 77 mW. The QCL mounted in the SH2 operates also at 20 °C and the NH_3 line is targeted with an injection current of 320 mA corresponding to a laser power of 59 mW. In addition, the selected laser driver provides both a slow triangular ramp current modulation to each laser to scan the selected absorption features, and a fast sinusoidal modulation. In this work, QEPAS measurements were performed in wavelength modulation and 2f-detection (WM-2f): for each SH, the laser sinusoidal modulation is set at half of the resonance frequency of its spectrophone, while the response is demodulated at its resonance frequency. The QTF current signals were converted into voltage signals by a transimpedance amplifier, with a 10 MΩ feedback resistor. The selected CB is equipped with an analog input terminal, allowing the acquisition and the on-board processing of the QTF signal. A custom-firmware was developed to detect the 2f-component of the signal, via a lock-in procedure and the data have been acquired with a time constant of 0.1 s. In the calibration phase of the sensor, the gas delivery system is composed of i) a gas mixer (MCQ Instrument Gas Blender GB1A30120164) whose output was connected to the input valve of the sensor box; ii) a pressure controller/flow meter (MKS Type 649); iii) a needle valve; and iv) and a vacuum pump (KNF N 813.4). The selected components were employed to stabilize the pressure and fix the gas flow at 50 sccm in the two SHs. The gas mixer is removed from the gas line for atmospheric measurements of the three gases, and the gas sample from outside will directly flow through the SHs.

3. SELECTION OF THE PRESSURE WORKING CONDITION

The developed sensor aims at detecting three important environmental gas species, i.e., methane, nitrous oxide, and ammonia. Since the performance of QEPAS sensors depends on the pressure working condition, the pressure dependence of the QEPAS signal was investigated for each target gas and the results are shown in Fig. 2. The amplitude and the frequency of sinusoidal modulation were optimized for each pressure value. For all three gases, certified concentrations in nitrogen matrix were flowed in the gas line.

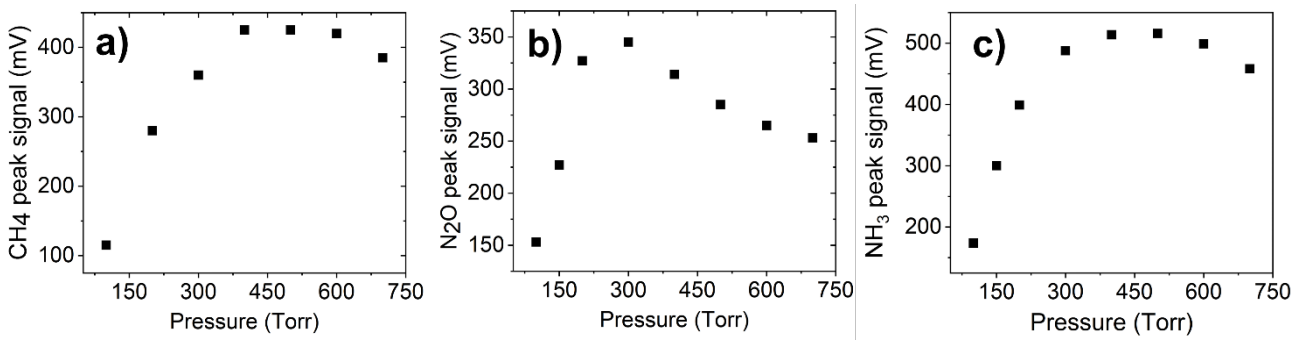

Fig. 2. a) CH_4 QEPAS signals as a function of the pressure when a mixture of 50 ppm of CH_4 in N_2 flows in the sensor box. b) N_2O QEPAS signal as a function of the pressure for a mixture of 10 ppm of N_2O diluted in N_2. c) NH_3 QEPAS signal acquired at different pressures for a mixture of 14 ppm of NH_3 in N_2

The methane peak signals measured for a mixture of 50 ppm of CH_4 in N_2 in the 100 – 700 Torr pressure range are shown in Fig. 2a. The highest QEPAS signal was measured at 500 Torr. In the same pressure range, the N_2O peak signal of a mixture containing 10 ppm of N_2O diluted in N_2 was measured and the results are show in Fig. 2b. The maximum signal was measured at 300 Torr, while a 18% reduction of the signal was recorded at 500 Torr. For a 14 ppm of NH_3 diluted in N_2, the SH2 response reaches its maximum value at 500 Torr. Differences in QEPAS signal-pressure trends can be mainly ascribed to different no-radiative relaxation rates of three gas species, which affecting the efficiency of the acoustic wave generation [23]. Since the two SHs have to be operated at the same pressure, we selected 500 Torr as operating pressure and all reported measurements in next paragraphs have been acquired under this condition. Consequently, the resonance properties of both spectrophones, in terms of resonance frequency and quality factor, were measured at 500 Torr. The SH1 spectrophone shown a resonance frequency of 12465.0 Hz and a quality factor of 15910, while the SH2 spectrophone resonated at 12467.6 Hz with a quality factor of 13180.

4. METHANE AND NITROUS OXIDE CALIBRATION WITH SENSOR HEAD 1

For methane and nitrous oxide calibrations, a cylinder containing pure N_2 was used to dilute a cylinder with a certified concentration of 10 ppm of CH_4 in N_2 and another one with a certified concentration of 10 ppm of N_2O in N_2, respectively. The QEPAS spectral scans of the selected CH_4 absorption lines was acquired in WM-2f by applying a sinusoidal current modulation with a peak-to-peak value of 10 mA. The same current modulation was applied to retrieve the N_2O absorption feature. Figs. 3a and 3b show the QEPAS spectral scans acquired for CH_4 and N_2O calibrations, respectively, in the 1 - 10 ppm concentration range.

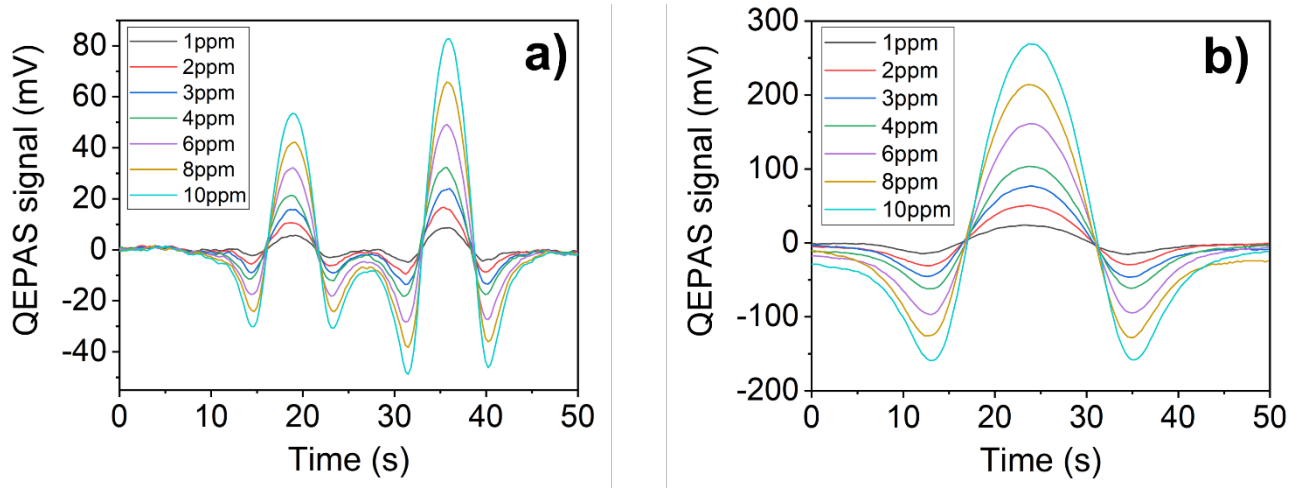

Fig. 3. a) QEPAS spectral scans measured for different CH_4:N_2 concentrations starting from a certified concentration of 10 ppm of CH_4 in N_2. b) N_2O QEPAS scans measured for 7 different N_2O:N_2 concentrations.

As expected from the HITRAN database, together with the most intense methane peak in the laser tuning range falling at 36 s, also the CH_4 peak at 1275.39 cm^{-1} is visible at 18 s. Hereafter, only the CH_4 peak falling at 1275.04 cm^{-1} will be considered for the analysis, since it allows higher sensitivity. The methane and nitrous oxide absorption features do not spectrally overlap in the laser tuning range, therefore the peak values of the QEPAS signals can be employed to measure the concentration of each gas in the mixture. The peak values were extracted from each spectral scan in Figs. 3a and 3b and plotted as a function of the related analyte concentration in Figs. 4a and 4b, respectively.

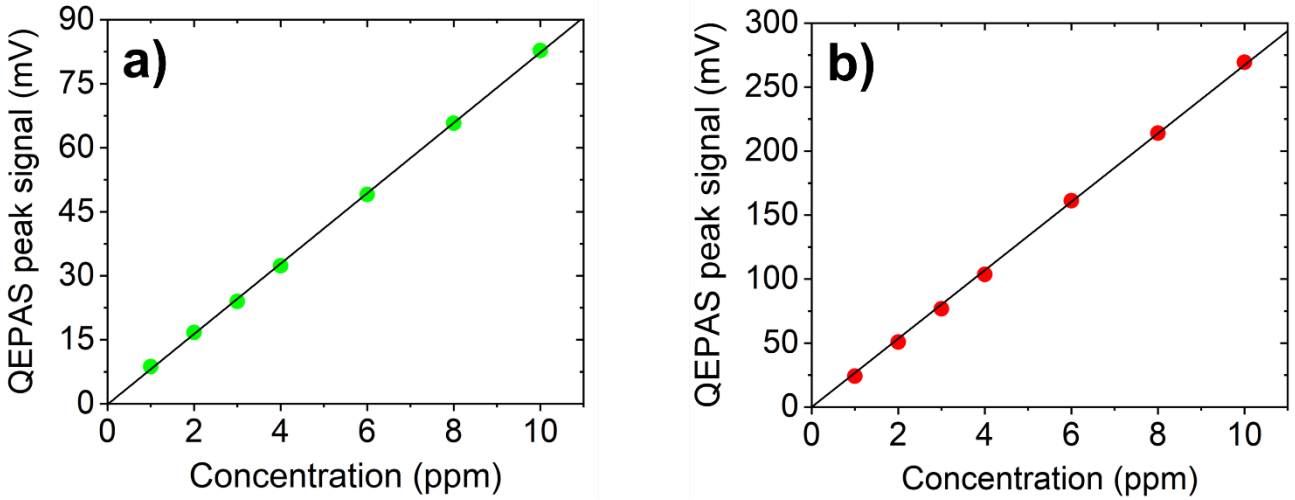

Fig. 4. a) Peak values measured for each methane concentration (green dots). The black solid line is the best linear fit of the experimental data. b) QEPAS peak signal as a function of N_2O concentration (red dots) with the corresponding best linear fit (black line).

As shown in Figs. 4a-b, the signal of both gases linearly depends on the analyte concentration. The linear fit of the two calibration curves yields a slope of 8.18 mV/ppm and 26.67 mV/ppm which represent the sensitivity for methane and nitrous oxide detection, respectively. The minimum detection limit (MDL) of the sensor was calculated as the ratio between the noise level and the sensitivity. The 1σ-noise level was measured as the standard deviation of the acquired data, when pure N_2 was flowing through SH1. With a 1σ-noise level of 230 μV at an integration time of 0.1 s, MDLs of 28.0 ppb and 8.6 ppb can be estimated for methane and nitrous oxide, respectively. The noise level can be lowered by further averaging the signal over longer times. An Allan-Werle deviation analysis was performed with the aim of estimating the 1σ noise

(and thus the achievable MDL) as a function of the lock-in integration time. The laser was locked far from both the absorption features while pure nitrogen flows in the SH1. The obtained Allan-Werle deviation plot is reported in Fig. 5.

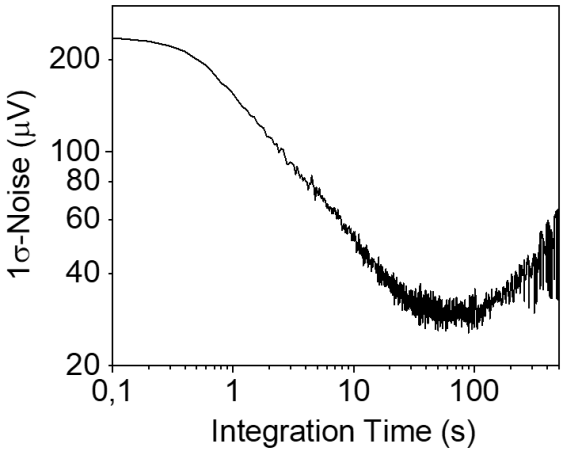

Fig. 5. Allan-Werle deviation plot of the QEPAS signal as a function of the lock-in integration time. For a 10 s integration time, the 1σ-noise level can be lowered to ~ 50 μV.

For a lock-in integration time of 10 seconds the 1σ-noise level can be lowered to ~ 50 μV, corresponding to minimum detection limits of 6 ppb and 2 ppb for CH_4 and N_2O, respectively. These detection sensitivities can be further improved by increasing the integration up to 30 seconds. For longer integration times, drift effects emerge, mainly induced by mechanical instabilities which causes a deterioration of the overall sensor head performance.

5. AMMONIA CALIBRATION WITH SENSOR HEAD 2

During the transport of a gas through a tube or cell, adsorption effects appear, especially in the case of polar molecules such as ammonia and water. Adsorption or desorption effects result in a change of the gas-phase concentration. Polar molecules such as NH_3 with large and permanent dipole moment have a strong tendency to stick to surfaces. The adsorption/desorption processes depend both on physical properties of the internal surface (material, temperature, porosity) and on experimental conditions (gas flow and analyte concentration) [24]. The internal wall surface of a sensor and tubes can be considered as a place with free binding sites for NH_3 molecules as well as a reservoir of molecules. Thereby, adsorption/desorption processes need to be considered for accurately determining the concentration of ammonia.
While a mixture is flowing within the sensor, an equilibrium condition can be achieved between the surface coverage and molecules concentration. Therefore, flowing a gas with a known concentration through a cell, the adsorption is quantified in terms of the time needed to reach a steady-state concentration. Conversely, when the gas species is removed from the gas line, molecules released from the reservoir will increase the number of molecules in the gas mixture (desorption process). In both cases, adsorption–desorption processes will negatively affect the accuracy of a gas detection technique.
The dynamic equilibrium between adsorption–desorption processes can be expressed by a qualitative theoretical model in terms of time and spatial derivatives of NH_3 concentration and surface coverage, i.e., the number of particles per area [25, 26]:

$$\frac{\partial c_g(x,t)}{\partial t} = -u\frac{\partial c_g(x,t)}{\partial x} - \frac{dS}{dV}\frac{\partial c_w(x,t)}{\partial t} \quad (1)$$

where c_g is the ammonia concentration in the gas mixture, c_w is the ammonia surface coverage, dS is the infinitesimal surface area, dV is the infinitesimal volume, u is the drift velocity of the gas mixture which can be expressed as the ratio between the flow velocity Φ and the cross-sectional area A, and x is the direction of flow, assumed to be rectilinear. Since the ammonia concentration is measured at the point $x = x_{meas}$, the Eq. 1 can be integrated from the entrance of the sensor system, $x = 0$, where the ammonia concentration is c^0_g to $x = x_{meas}$, where a concentration c^m_g is measured, leading to:

$$\frac{\partial c_g^m(t)}{\partial t} = \frac{\Phi}{V}\left[c_g^0 - c_g^m\right] - \frac{S}{V}\frac{\partial c_w(x,t)}{\partial t} \quad (2)$$

The factor Φ/V is the inverse of the characteristic gas-exchange time τ_0. $\partial c_w/\partial t$ represents the effective adsorption rate, namely the difference between the adsorption rate and the desorption rate. $\partial c_w/\partial t$ can be expressed in the form of a dynamic exchange of molecules between the surface and the gas by separating the two contributions. If the surface wall coverage saturation is c_{w0}, the molecules of gas lost to the surface per unit time (adsorption) can be assumed proportional to the density of free binding sites on the surface, $c_{w0} - c_w$, while the number leaving the surface per unit time (desorption) is proportional to the density of occupied sites c_w:

$$\frac{\partial c_w}{\partial t} = k_1(c_{w0} - c_w) - k_2 c_w \quad (3)$$

where k_1 and k_2 are the proportionality constants. With this formulation, adsorption and desorption can be separated. This allows the identification of two distinguishable situations: i) the sensor contains no ammonia and at a certain time a gas mixture with a fixed ammonia concentration c_0 starts to flow inside (sensor filling); ii) the sensor contains a mixture with fixed concentration of ammonia c_0 and a certain point it is pumped out by fluxing pure N_2 (sensor cleaning). It is safe to assume that the desorption is negligible during sensor filling and, conversely, the adsorption can be neglected during the sensor cleaning. For sensor filling, Eq. 3 becomes:

$$\left(\frac{\partial c_w}{\partial t}\right)_f = k_1(c_{w0} - c_w) \quad (4)$$

which has as solution:

$$c_w(t)|_f = c_{w0}\left(1 - e^{-\frac{t}{\tau_1}}\right) \quad (5)$$

where $\tau_1 = 1/k_1$. By combing Eq. 2 and 5 and imposing the boundary condition $c^m_g(0) = 0$ and $c^0_g = c_0$, $c^m_g(t)|_f$ can be expressed as:

$$c_g^m(t)\big|_f = A_0\left(1 - e^{-\frac{t}{\tau_0}}\right) + A_1\left(1 - e^{-\frac{t}{\tau_1}}\right) \quad (6)$$

where:

$$A_1 = \frac{S \cdot c_{w0}}{\Phi(\tau_1 - \tau_0)} \quad (7)$$

and $A_0 = c_0 - A_1$.
For sensor cleaning, the first term of right-hand side of Eq. 3 can be neglected and its solution is:

$$c_w(t)|_c = c_{w0}\, e^{-\frac{t}{\tau_2}} \quad (8)$$

where $\tau_2 = 1/k_2$. Again, by combing Eq. 2 and 8 and imposing the boundary condition $c^m_g(0) = c_0$ and $c^0_g = 0$, the $c^m_g(t)|_c$ can be expressed as:

$$c_g^m(t)\big|_c = A_2\left(1 - e^{-\frac{t}{\tau_0}}\right) - A_3\left(1 - e^{-\frac{t}{\tau_2}}\right) \quad (9)$$

with:

$$A_3 = \frac{S \cdot c_{w0}}{\Phi(\tau_2 - \tau_0)} \quad (10)$$

and $A_2 = c_0 - A_3$.
To estimate τ_0, τ_1 and τ_2, a cylinder with certified concentration of 14 ppm of NH_3 in N_2 and a cylinder with pure N_2 were used as channel inputs to the gas blender. The situation of sensor filling was realized starting with a pure N_2 flowing inside

the sensor box: at a certain time (corresponding to $t = 0$ of the theoretical model) a fast-switching interrupts the N_2 flows and the certified mixture of NH_3 starts to flow. Conversely, the sensor cleaning starts with the certified mixture of NH_3 and moves to a fast switch at $t = 0$ to the pure N_2. In both cases, the laser current was locked to NH_3 absorption peak while the sinusoidal modulation is applied with a peak-to-peak current of 15 mA, in WM-2f detection. The NH_3 QEPAS signal normalized to the unit as a function of time during the filling and cleaning procedure is reported in Figs. 6a and 6b, respectively.

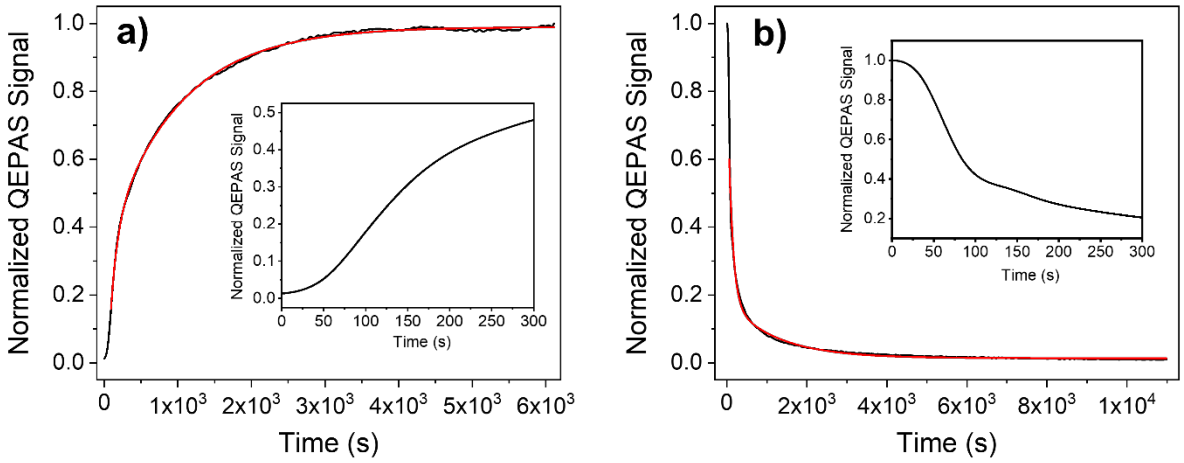

Fig. 6. a) Normalized QEPAS signal as function of time acquired locked on NH_3 absorption peak during filling step (black curve) together with the performed exponential fit (red curve) based on Eq.6. Inset: zoom on the inflection point observed in the initial signal rise. b) Normalized QEPAS signal as function of time acquired locked on NH_3 absorption peak during cleaning step (black curve) together with the performed exponential fit (red curve) based on Eq.9. Inset: zoom on the inflection point observed in the initial signal decrease.

As shown in the inset of Fig. 6a, the initial signal rise has a positive concavity until $t = 92$ s where there is an inflection point. Thus, for $t < 92$ s, the QEPAS signal rises more slowly than that predicted by Eq. 6, suggesting the presence of nonlinear effects that are not included in the simplified theoretical model [25]. This initial QEPAS signal behavior can be ascribed to the starting huge density of free binding sites on the sensor inner surfaces, consequently the probability for NH_3 molecules to be captured is very high and few molecules reach the measurement point, i.e., the spectrophone. When these sites start to be filled, the NH_3 molecules more easily reach the spectrophone and a dynamic equilibrium between the gas flux and the adsorption processes can be established, which is the condition imposed by the theoretical model during the transient. A similar situation is also observed in the sensor cleaning process: the QEPAS signal decrease looks like delayed until $t = 60$ s, then the signal drops down with a positivity concavity, as predicted by Eq. 9. Based on these considerations, only experimental data beyond the inflection points were fitted by using Eq. 6 and Eq. 9 and reported as solid red line in Fig. 6a and Fig. 6b for the filling and cleaning processes, respectively. The fitting procedure gives $\tau_0 = 93$ s and $\tau_1 = 966$ s for the filling procedure and of $\tau_0 = 107$ s and $\tau_2 = 1212$ s for the cleaning procedure. In both cases, the time constant related to adsorption/desorption processes is more than one order of magnitude higher than the characteristic gas-exchange time τ_0, which is related only to the dimensions of the sensor and the gas flow. These obtained results were employed to accurately calibrate the sensor.

The calibration of SH2 for NH_3 was performed as for SH1, starting from the certified concentration of 14 ppm of NH_3 in N_2. For each dilution, a waiting time of 60 minutes for reaching a steady-state signal was considered. After that, the sensor was cleaned before moving to the next dilution. The QEPAS scans referred to different NH_3 concentrations in N_2 are reported in Fig. 7a.

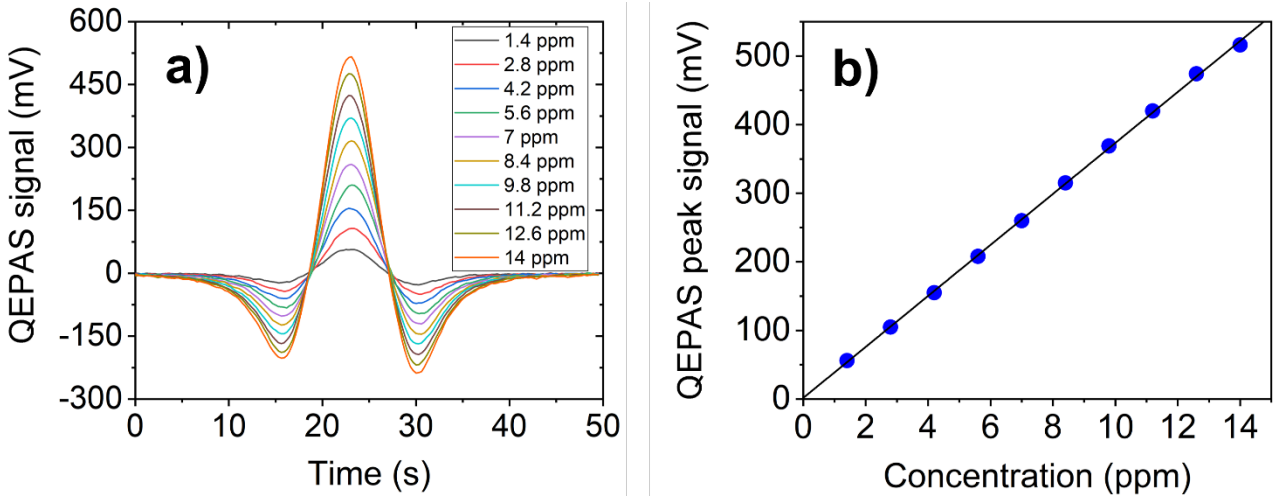

Fig. 7. a) *2f*-QEPAS spectra collected by varying the NH_3 concentration within the gas cell. b) QEPAS peak signals extracted from spectral scans reported as function of NH_3 concentration (blue dots). The performed best linear fit is superimposed to the collected data (black line)

The peak values are plotted as a function of the NH_3 concentration in Fig. 7b, together with the linear fit which returns a sensitivity of 37.22 mV/ppm, corresponding to an MDL of 5.8 ppb (1σ-noise level of 210 μV) at an integration time of 0.1 s. The Allan-Werle analysis of the 1σ noise level is reported in Fig. 8.

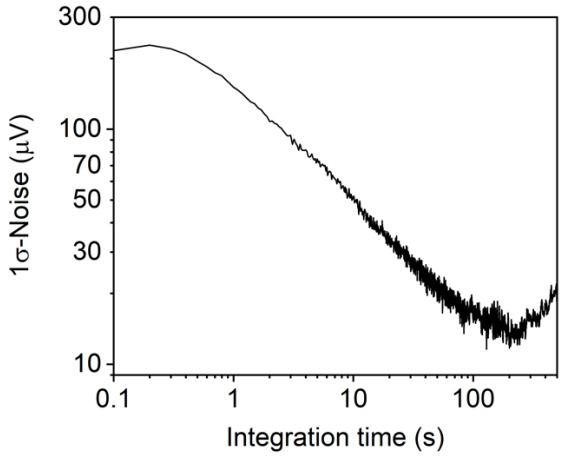

Fig. 8. Allan-Werle deviation analysis for NH_3 sensor. The estimated 1σ-noise level is reported as a function of sensor integration time.

The noise level can be lowered to 50 μV when the signal integration time is increased to 10 s and consequently the minimum detection limit reaches 1.4 ppb.

6. MEASUREMENT OF ATMOSPHERIC AMMONIA, METHANE AND NITROUS OXIDE

The MDLs reached for the three gas species at an integration time of 0.1 s are below the natural abundance of the three analytes, thus making SH1 and SH2 suitable for the monitoring of their levels in environmental air. The sensor was employed to measure the concentrations of methane, nitrous oxide, and ammonia in laboratory air for more than 4 hours. A software was developed to drive both sensor heads and acquire and process the QEPAS signals. The measurements were performed by acquiring QEPAS spectral scans of the CH_4 and N_2O absorption lines with SH1 and the QEPAS spectral of the NH_3 absorption line with SH2, both operating at 0.1 s integration time. For each spectral scan, the QEPAS peak signals of CH_4, N_2O, and NH_3 absorption features were extracted and are plotted as a function of time in Fig. 9. The time interval between two consecutive peaks of the same analyte was 50 s. The reported concentrations were calculated using the calibration of each analyte, reported in Figs. 4a-b and Fig. 7b.

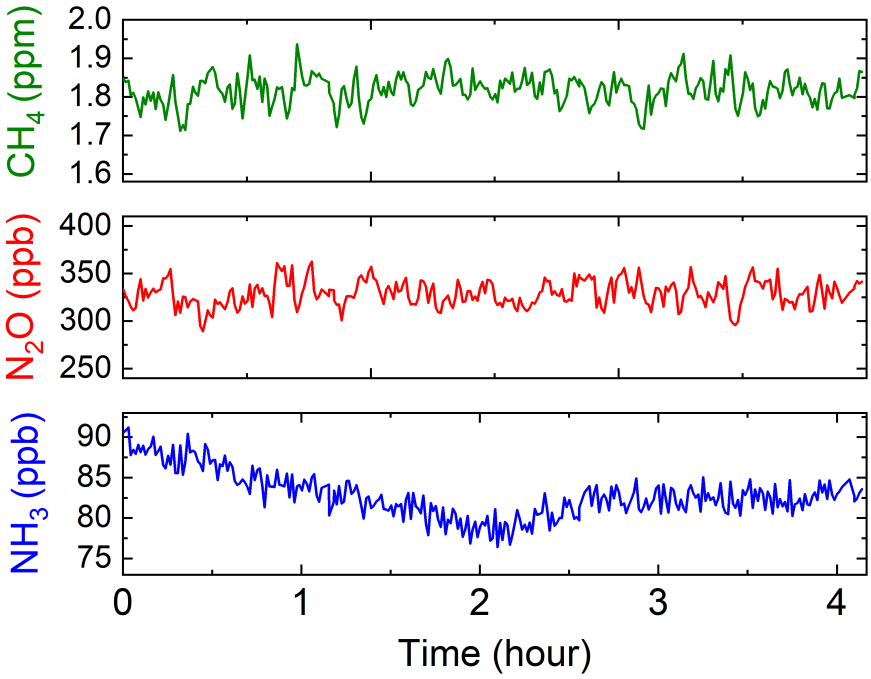

Fig. 9. QEPAS peak signals extracted by consecutive QEPAS spectra acquired by sampling the air inside the laboratory. SH1 was used to monitor CH_4 (green line) and N_2O (red line) concentrations, while sensor SH2 was used to detect NH_3 (blue line).

The extracted peaks returned stable concentrations of methane and nitrous oxide, with an average CH_4 concentration of 1.81 ppm, with a standard deviation of 0.04 ppm, and an average N_2O concentration of 329 ppb, with a standard deviation of 13 ppb. These measured values are consistent with the expected CH_4 and N_2O levels in atmosphere [27]. The ammonia concentration slightly varied during the measurement period, with an average level of 83 ppb and a standard deviation of 3 ppb. This NH_3 level is coherent with the typical levels of ammonia in indoor air [5].

7. CONCLUSIONS

In this work, we reported on a portable QEPAS 19-inches 6U-rack sensor system capable to detect methane, nitrous oxide, and ammonia, three important analytes for the study of the environmental footprint of agriculture and food production industry. The realized QEPAS sensor is composed of two sensor heads, connected in series. The first sensor head is equipped with a QCL, capable to target two adjacent absorption features of CH_4, centered at 1275.04 cm^{-1} and 1275.39 cm^{-1}, and an absorption feature of N_2O, centered at 1275.49 cm^{-1}. A QCL capable to detect the NH_3 absorption feature at 1103.44 cm^{-1} was selected and mounted in SH2. The same type of spectrophone, composed of a 12 kHz T-shaped QTF coupled with optimized resonator tubes, was employed in both sensor heads. At an integration time of 0.1 s, the CH_4 and

N_2O minimum detection limits were 28.0 ppb and 8.6 ppb, respectively. Since ammonia is a polar molecule with large and permanent dipole moment, adsorption/desorption processes were modelled and considered for an accurate calibration of the sensor. An NH_3 minimum detection limit of 5.8 ppb at an integration time of 0.1 s was obtained, considering a waiting time of 60 minutes between each concentration in the calibration phase. The sensor was employed to monitor the concentration of CH_4, N_2O and NH_3 in laboratory air, since the achieved detection limits were all below the natural abundance of the three gas species in atmosphere. This measurement returned an average CH_4 concentration of 1.81 ppm, an average N_2O concentration of 329 ppb and an average NH_3 concentration of 83 ppb. These results are compatible with the expected levels of these analytes in indoor air. Considering the obtained performances and the lab test, the realized sensor results suitable for the on-field monitoring of gas traces of methane, nitrous oxide and ammonia for agriculture and food production industry applications.

CREDIT AUTHORSHIP CONTRIBUTION STATEMENT

Giansergio Menduni: Conceptualization, Methodology, Writing - Original Draft, Writing - Review & Editing. **Andrea Zifarelli:** Methodology, Writing - Original Draft, Formal analysis, Visualization. **Elena Kniazeva:** Validation, Formal analysis, Investigation, Data Curation. **Stefano Dello Russo:** Validation, Formal analysis, Investigation, Data Curation. **Pietro Patimisco:** Writing - Original Draft, Writing - Review & Editing, Visualization, Supervision, Project administration. **Angelo Sampaolo:** Writing - Review & Editing, Supervision, Project administration. **Marilena Giglio:** Writing - Review & Editing, Supervision, Project administration. **Fabrizio Manassero:** Writing - Review & Editing, Project administration. **Elio Dinuccio:** Writing - Review & Editing, Project administration. **Giorgio Provolo:** Writing - Review & Editing, Project administration. **Vincenzo Spagnolo:** Writing - Review & Editing, Supervision, Project administration, Funding acquisition.

DECLARATION OF COMPETING INTEREST

The authors declare that they have no competing interests.

ACKNOWLEDGMENTS

Authors from Dipartimento Interateneo di Fisica di Bari acknowledge funding from the European Union's Horizon 2020 Research and Innovation Program under grant agreement No. 101016956 PASSEPARTOUT and the financial support from the European Union's Horizon 2020 Research and Innovation Program under the Marie Skłodowska-Curie project OPTAPHI, grant No. 860808.

REFERENCES

[1] T. M. Letcher, Introduction With a Focus on Atmospheric Carbon Dioxide and Climate Change, in: T.M. Letcher (Ed.), Future energy, Elsevier, Amsterdam, 2020, 3–17. https://doi.org/10.1016/B978-0-08-102886-5.00001-3.

[2] S. Das, W. Wang, S. Reeves, R. C. Dalal, Y. P. Dang, A. Gonzalez, P. M. Kopittke, Non-target impacts of pesticides on soil N transformations, abundances of nitrifying and denitrifying genes, and nitrous oxide emissions, Science of The Total Environment 844 (2022), 157043. https://doi.org/10.1016/j.scitotenv.2022.157043.

[3] F. N. Tubiello, M. Salvatore, A. F. Ferrara, J. House, S. Federici, S. Rossi, R. Biancalani, R. D. C. Golec, H. Jacobs, A. Flammini, P. Prosperi, P. Cardenas-Galindo, J. Schmidhuber, M. J. S. Sanchez, N. Srivastava, P. Smith, The Contribution of Agriculture, Forestry and other Land Use activities to Global Warming, 1990–2012, Global Change Biology 21(7) (2015) 2655–2660. https://doi.org/10.1111/gcb.12865.

[4] S. C. Vac, G. E. Popit¸, N. Frunzeti, A. Popovici, Evaluation of Greenhouse Gas Emission from Animal Manure Using the Closed Chamber Method for Gas Fluxes, Not. Bot. Horti Agrobot. Cluj-Napoca 41 (2013) 576–581. https://doi.org/10.15835/nbha4129259.

[5] M. Li, C. J. Weschler, G. Bekö, P. Wargocki, G. Lucic, J. Williams, Human Ammonia Emission Rates under Various Indoor Environmental Conditions, Environ. Sci. Technol. 54 (2020) 5419−5428. https://doi.org/10.1021/acs.est.0c00094.
[6] F. J. Dentener, P. J. Crutzen, A three-dimensional model of the global ammonia cycle, J. Atmos. Chem. 19 (1994) 331–369. https://doi.org/10.1007/BF00694492.
[7] W. A. H. Asman, Factors influencing local dry deposition of gases with special reference to ammonia, Atmos. Environ. 32(3) (1998) 415–421. https://doi.org/10.1016/S1352-2310(97)00166-0.
[8] G. H. Mount, B. Rumbur, J. Having, B. Lamb, H. Westberg, D. Yonge, K. Johnson, R. Kincaid, Measurement of atmospheric ammonia at a dairy using differential optical absorption spectroscopy in the mid-ultraviolet, Atmos. Environ. 36(11) (2002) 1799-1810. https://doi.org/10.1016/S1352-2310(02)00158-9.
[9] J. Hodgkinson, R. P. Tatam, Optical gas sensing: A review, Meas. Sci. Technol. 24 (2013), 012004. https://doi.org/10.1088/0957-0233/24/1/012004.
[10] W. Ren, W. Jiang, F. K. Tittel, Single-QCL-based absorption sensor for simultaneous trace-gas detection of CH_4 and N_2O, Appl. Phys. B 117(1) (2014) 245–251. https://doi.org/10.1007/s00340-014-5828-8.
[11] L. Dong, F. K. Tittel, C. Li, N. P. Sanchez, H. Wu, C. Zheng, Y. Yu, A. Sampaolo, R. J. Griffin, Compact TDLAS based sensor design using interband cascade lasers for mid-IR trace gas sensing, Opt Express 24(6) (2016) A528–A535. https://doi.org/10.1364/OE.24.00A528.
[12] T. I. Yacovitch, S. C. Herndon, J. R. Roscioli, C. Floerchinger, R. M. McGovern, M. Agnese, G. Pétron, J. Kofler, C. Sweeney, A. Karion, S. A. Conley, E. A. Kort, L. Nähle, M. Fischer, L. Hildebrandt, J. Koeth, J. B. McManus, D. D. Nelson, M. S. Zahniser, C. E. Kolb, Demonstration of an Ethane Spectrometer for Methane Source Identification, Environ. Sci. Technol. 48(14) (2014) 8028–8034. https://doi.org/10.1021/es501475q.
[13] A. Elia,P. M. Lugarà, C. Di Franco, V. Spagnolo, Photoacoustic Techniques for Trace Gas Sensing Based on Semiconductor Laser Sources, Sensors 9 (2009) 9616–9628. https://doi.org/10.3390/s91209616.
[14] A. A. Kosterev, Y. A. Bakhirkin, R. F. Curl, F. K. Tittel, Quartz-enhanced photoacoustic spectroscopy, Opt. Lett. 27 (2002) 1902–1904. https://doi.org/10.1364/OL.27.001902.
[15] P. Patimisco, A. Sampaolo, L. Dong, F.K. Tittel, V. Spagnolo, Recent advances in quartz enhanced photoacoustic sensing, App. Phys. Rev. 5 (2018) 011106. https://doi.org/10.1063/1.5013612.
[16] S. Viciani, M. Siciliani de Cumis, S. Borri, P. Patimisco, A. Sampaolo, G. Scamarcio, P. De Natale, F. D'Amato, V. Spagnolo, A quartz-enhanced photoacoustic sensor for H_2S trace-gas detection at 2.6 μm, Appl. Phys. B 119 (2014) 21-27. https://doi.org/10.1007/s00340-014-5991-y.
[17] P. Patimisco, A. Sampaolo, H. Zheng, L. Dong, F.K. Tittel, V. Spagnolo, Quartz-enhanced photoacoustic spectrophones exploiting custom tuning forks: a review, Advances in Physics X 2 (2016) 169-187. https://doi.org/10.1080/23746149.2016.1271285.
[18] S. Dello Russo, M. Giglio, A. Sampaolo, P. Patimisco, G. Menduni, H. Wu, L. Dong, V. M. N. Passaro, V. Spagnolo, Acoustic Coupling between Resonator Tubes in Quartz-Enhanced Photoacoustic Spectrophones Employing a Large Prong Spacing Tuning Fork, Sensors 19 (2019) 4109. https://doi.org/10.3390/s19194109.
[19] G. Menduni, A. Sampaolo, P. Patimisco, M. Giglio, Dello Russo S., A. Zifarelli, A. Elefante, P. Z. Wieczorek, T. Starecki, V. M. N. Passaro, F. K. Tittel, V. Spagnolo, Front-end amplifiers for tuning forks in quartz enhanced photoacoustic spectroscopy, Applied Sciences 10(8) (2020) 2947. https://doi.org/10.3390/app10082947.
[20] M. Giglio, A. Elefante, P. Patimisco, A. Sampaolo, F. Sgobba, H. Rossmadl, V. Mackowiak, H. Wu, F. K. Tittel, L. Dong, V. Spagnolo, Quartz-enhanced photoacoustic sensor for ethylene detection implementing optimized custom tuning fork-based spectrophone, Optics Express 27 (2019) 4271-4280. https://doi.org/10.1364/OE.27.004271.
[21] P. Patimisco, A. Sampaolo, M. Giglio, S. Dello Russo, V. Mackowiak, H. Rossmadl, A. Cable, F. K. Tittel, V. Spagnolo, Tuning forks with optimized geometries for quartz-enhanced photoacoustic spectroscopy, Optics Express 27 (2019) 1401-1415. https://doi.org/10.1364/OE.27.001401.
[22] I. E. Gordon, L. S. Rothman, R. J. Hargreaves, R. Hashemi, E. V. Karlovets, F. M. Skinner, E. K. Conway, C. Hill, R. V. Kochanov, Y. Tan, P. Wcisło, A. A. Finenko, K. Nelson, P. F. Bernath, M. Birk, V. Boudon, A. Campargue, K. V. Chance, A. Coustenis, B. J. Drouin, J. M. Flaud, R. R. Gamache, J. T. Hodges, D. Jacquemart, E. J. Mlawer, A. V. Nikitin, V. I. Perevalov, M. Rotger, J. Tennyson, G. C. Toon, H. Tran, V. G. Tyuterev, E. M. Adkins, A. Baker, A. Barbe, E. Canè, A. G. Császár, A. Dudaryonok, O. Egorov, A. J. Fleisher, H. Fleurbaey, A. Foltynowicz, T. Furtenbacher, J. J. Harrison, J. M. Hartmann, V. M. Horneman, X. Huang, T. Karman, J. Karns, S. Kassi, I. Kleiner, V. Kofman, F. Kwabia-Tchana, N. N. Lavrentieva, T. J. Lee, D. A. Long, A. A. Lukashevskaya, O. M. Lyulin, V. Y. Makhnev, W. Matt, S. T. Massie, M. Melosso, S. N. Mikhailenko, D.

Mondelain, H. S. P. Müller, O. V. Naumenko, A. Perrin, O. L. Polyansky, E. Raddaoui, P. L. Raston, Z. D. Reed, M. Rey, C. Richard, R. Tóbiás, I. Sadiek, D. W. Schwenke, E. Starikova, K. Sung, F. Tamassia, S. A. Tashkun, J. Vander Auwera, I. A. Vasilenko, A. A. Vigasin, G. L. Villanueva, B. Vispoel, G. Wagner, A. Yachmenev, S. N. Yurchenko, The HITRAN2020 molecular spectroscopic database, J. Quant. Spectrosc. Radiat. Transf. 277 (2022) 107949. https://doi.org/10.1016/j.jqsrt.2021.107949.

[23] S. Dello Russo, A. Sampaolo, P. Patimisco, G. Menduni, M. Giglio, C. Hoelzl, V.M.N. Passaro, H. Wu, L. Dong, V. Spagnolo, Quartz-enhanced photoacoustic spectroscopy exploiting low-frequency tuning forks as a tool to measure the vibrational relaxation rate in gas species, Photoacoustics 21 (2021) 100227. https://doi.org/10.1016/j.pacs.2020.100227.

[24] O. Vaittinen, M. Metsälä, S. Persijn, M. Vainio, L. Halonen, Adsorption of ammonia on treated stainless steel and polymer surfaces, Appl. Phys. B. 115 (2014) 185-196. https://doi.org/10.1007/s00340-013-5590-3.

[25] J. Henningsen, N. Melander, Sensitive measurement of adsorption dynamics with nonresonant gas phase photoacoustics, Appl. Opt. 36 (1997) 7037-7045. https://doi.org/10.1364/AO.36.007037.

[26] A. Schmohl, A. Miklos, P. Hess, Effects of adsorption–desorption processes on the response time and accuracy of photoacoustic detection of ammonia, Appl. Opt. 40 (2001) 2571-2578. https://doi.org/10.1364/ao.40.002571.

[27] United States Environmental Protection Agency, Inventory of U.S. Greenhouse Gas Emissions and Sinks: 1990-2018. https://www.epa.gov/ghgemissions/inventory-us-greenhouse-gas-emissions-and-sinks-1990-2018, 2020 (accessed 17 July 2022).